75th International Astronautical Congress (IAC), Milan, Italy, 14-18 October 2024.

IAC-24, A6, 7, 2, x87463

Validation of a Fuel-Efficient Collision Avoidance Manoeuvre Optimiser for the GRACE-FO Mission.

Andrea Zollo[a*], Zeno Pavanello[b], Roberto Armellin[b], Juan Félix San Juan Díaz[c], Benjamin Schlepp[a] and Ralph Kahle[a]

[a]*German Space Operation Centre (GSOC), DLR, Münchener Str. 20, 82234, Weßling, Germany, email: {andrea.zollo, benjamin.schlepp, ralph.kahle}@dlr.de*
[b]*Te Pūnaha Ātea - Space Institute, The University of Auckland, 20 Symonds Street, 1010, Auckland, New Zealand, email: roberto.armellin@auckland.ac.nz, zpav176@aucklanduni.ac.nz*
[c]*Scientific Computation & Technological Innovation Center, University of La Rioja, Madre de Dios 53, 26006, Logroño, La Rioja, Spain, email: juanfelix.sanjuan@unirioja.es*
[*]Corresponding Author: andrea.zollo@dlr.de

Abstract

In recent decades, the increasing number of objects in Earth's orbit has raised significant safety concerns for spacecraft operations. Particularly in Low Earth Orbit (LEO), missions are experiencing a rise in manoeuvre frequency to maintain safety and operational continuity, mitigating the risk of colliding with hazardous objects. In this framework, it is crucial to design, develop and maintain tools to compute fuel-efficient collision avoidance manoeuvres (CAMs) in order to aid operators' tasks while gradually minimizing the need for human intervention and advancing towards spacecraft autonomy. Recent research efforts by the authors have focused on computing fuel-optimal CAMs using convex optimisation. The dual objective is to minimize overall fuel consumption while respecting safety conditions based on the probability of collision (PoC) reduction. Specifically, the approach combines sequential convex programming, second-order cone programming, lossless convexification, and differential algebra to approximate the non-convex optimal control problem progressively.

The aim of this study is to validate the convex CAM optimiser in the context of a real mission, incorporating operational constraints that are specifically tailored for the US-German joint close-formation mission Gravity Recovery and Climate Experiment - Follow-On (GRACE-FO), operated by the German Space Operations Center (GSOC) of DLR. The mission represents an ideal test-bench for the CAM optimiser. The previously established methodology is, in fact, improved by including constraints on the target relative orbital elements to facilitate formation re-acquisition post-manoeuvre. The convex optimiser's output is tested and validated against actual CAMs executed throughout the mission's duration, achieving enhanced fuel efficiency in terms of Delta-V, manoeuvre timing, and risk reduction. Moreover, the optimiser's computational time significantly outperforms the time typically taken by operators to implement CAM strategies.

Keywords: Collision Avoidance manoeuvre, Trajectory Optimisation, Convex Optimisation, Spacecraft Operations, Formation-flying, Space Situational Awareness.

1. Introduction

Over the past decades, Earth's orbital environment has become increasingly hazardous for safe spacecraft operations due to a dramatic rise in the debris population [1]. This situation has become significantly more urgent with the saturation of the most commonly used orbital regimes and the emergence of mega-constellations in the space sector. Consequently, spacecraft operators are experiencing more frequent close encounter alerts, necessitating more manoeuvres to ensure safety and operational continuity and to mitigate the risk of collisions with hazardous objects.

Collision avoidance operations are a vital activity for control centres, where accuracy and timing are crucial. These operations are typically divided into three major parts. The first is the conjunction risk assessment, an operational process that evaluates the severity of a close approach. The subsequent set of activities is triggered only when a close approach is deemed critical, involving the preparation and execution of a collision avoidance manoeuvre (CAM). During this stage, a manoeuvre is typically planned to reduce the PoC and uploaded to the spacecraft at the nearest opportunity provided by the ground station network, before the time of closest approach (TCA). During the execution of a CAM, the mission is normally interrupted as the spacecraft must temporarily deviate from its operational orbit and/or orientation. For this reason, a third sequence of ground activities is undertaken to bring the spacecraft back to mission configuration. Assessing the criticality of an event

is typically a well-established procedure, with Flight Dynamics Systems (FDS) equipped with algorithms to aid in decision-making [2]. However, the responsibility for planning and executing a CAM, as well as subsequent activities to return the spacecraft to nominal configuration, always rests with ground operators. CAM planning for different missions is performed on a case-by-case basis and requires manual intervention most of the time. The recent rise in CAM frequency, particularly for missions in low Earth orbit (LEO), has thus highlighted the need to develop and maintain tools capable of autonomously computing fuel-efficient CAMs with minimal human intervention. These tools must be robust in challenging environments and specifically designed to accommodate the operational constraints of each mission.

Significant effort has been made by the authors in the direction of optimally computing CAMs. Traditionally, the main objective of optimisers of such kind is to minimize the Δv while reducing PoC or increasing the miss distance to a safe threshold. In its discretised form, the continuous thrust CAM optimisation problem falls under the category of non-linear programming (NLP) due to the non-linear nature of the objective function, the dynamical model, and the metrics characterizing the close approach. Additionally, the PoC constraints are non-convex. Within the context of this work, the authors are solving the non-convex challenges of the optimal control problem by progressively approximating it in a convex one. The specifics of the optimisation method are detailed in references [3–5]: the nonlinearity of the objective function is tackled by introducing slack variables and applying lossless convexification techniques [6–8]; the conjunction dynamics is instead linearised with the use of differential algebra (DA), which allows for the automatic linearization of the motion under any dynamics; the PoC constraint is turned into a linearized squared Mahalanobis distance (SMD) constraint by means of a projection and linearization algorithm [9]. The original multi-impulsive formulation of the method [8] has been extensively enhanced to address various CAM design scenarios using a low-thrust formulation, including long-term [3] and multiple encounters [5], as well as conjunctions occurring during continuously propelled orbit transfers [4]. This paper aims to further develop this line of research by adapting the existing methodology to real CAM scenarios from an ongoing mission where the current algorithm lacks direct applicability. Significant efforts, such as those in [10, 11], address mission-imposed constraints, but they remain quite general and are not specifically tailored to a particular mission. Specifically, the formulation in reference [10] is more tailored for Multi-Criteria decisions, while [11] propose a multi-objective optimiser that is not completely efficient for CAM computation. Reference [12], on the other hand, remarkably incorporates station-keeping constraints by defining a target box for the post-manoeuvre state and enforcing that the semi-major axis difference relative to this box is zero at the final time. Despite this, its formulation employs Linear Programming (LP), which makes the method less accurate than that of a convex optimiser. Within the context of this work, we are incorporating operational constraints in the CAM solver specifically tailored for the US-German joint close-formation mission Gravity Recovery and Climate Experiment-Follow-On (GRACE-FO), operated by the German Space Operations Center (GSOC) of the German Aerospace Center (DLR). This mission consists of two twin Spacecrafts that are controlled in close formation with an along-track distance kept within the range 220 ± 50 km (more details of the mission are provided in Section 2). The intrinsic mission requirements for controlling the formation present a challenging scenario to test the optimiser's performance. Specifically, we consider formation-keeping constraints such as separation distance, relative altitude, and target mean semi-major axis and eccentricity differences. The approach is validated using a real test case scenario with the support of GSOC/FDS algorithms specifically designed for formation control monitoring. The optimised manoeuvre is compared in terms of processes and performance to an actual CAM executed by the GRACE-FO Flight Dynamics operators. Additionally, the optimiser is tested in a real multiple conjunction scenario encountered by operators during ground operations earlier this year.

The paper is structured as follows. Section 2 gives an overview of the GRACE-FO mission and how the formation is controlled. Section 3 recaps the mathematical background and implementation of the optimiser developed in [3–5, 8], and it additionally presents the operational constraints added to the formulation. Section 4 shows the test cases and the validation of the optimised solution. Conclusions are drawn in Section 5.

2. GRACE-Follow-On mission

Launched in May 2018, the GRACE-FO mission carries on the legacy of the original GRACE mission, which began in 2002 and operated for 14 years before being decommissioned. Like its predecessor, GRACE-FO was developed by NASA and the German Research Centre for Geoscience (GFZ) and is currently operated by the German Space Operations Center (GSOC) of DLR. The mission consists of two identical spacecraft, GRACE-FO1 (GF1) and GRACE-FO2 (GF2), built by Airbus Defence and Space. They are positioned in a polar, nearly circular orbit at an altitude of 500 km. The spacecraft are flying in close formation with an average separation of 220 ± 50 km. Both satellites are equipped with laser ranging interferometers (LRI), which precisely measure their inter-satellite range. Variations in this distance are

linked to changes in Earth's mass distribution, such as the presence of mountain ranges or underground water reservoirs. As Earth's gravitational pull alters the distance between the satellites, scientists can calculate these changes to detect shifts in mass distribution with remarkable precision. GRACE and GRACE-FO missions revolutionized our understanding of the global water cycle, revealing monthly variations in liquid water and ice masses. It also contributed to our knowledge of large-scale changes in Earth's solid structure, enhancing scientific understanding of Earth's gravitation models and improving the accuracy of environmental monitoring and forecasting. For the interested reader, a way more detailed overview of the mission can be found in [13].

2.1 Formation Relative Motion and Control

The motion of the deputy satellite (GF2) relative to the main reference spacecraft (GF1) can be described using the theory developed in [14]. Given the osculating Cartesian states of GF1 and GF2, denoted as $\boldsymbol{x}_1$ and $\boldsymbol{x}_2 \in \mathbb{R}^6$ at time $t \in \mathbb{R}$, the mean relative orbital elements $\Delta\boldsymbol{p}$ can be computed through a nonlinear transformation $\boldsymbol{g}(\cdot) : \mathbb{R}^6 \times \mathbb{R}^6 \to \mathbb{R}^6$:

$$\Delta\boldsymbol{p} = \boldsymbol{g}(\boldsymbol{x}_1, \boldsymbol{x}_2), \tag{1}$$

In general, the vector $\Delta\boldsymbol{p} \in \mathbb{R}^6$ can be expressed as a function of the mean orbital elements of the two spacecraft

$$\begin{bmatrix} \Delta a \\ a\Delta e_x \\ a\Delta e_y \\ a\Delta i_x \\ a\Delta i_y \\ a\Delta\psi \end{bmatrix} = \begin{bmatrix} a_2 - a_1 \\ a_1(e_2\cos(\omega_2) - e_1\cos(\omega_1)) \\ a_1(e_2\sin(\omega_2) - e_1\sin(\omega_1)) \\ a_1(i_2 - i_1) \\ a_1(\Omega_2 - \Omega_1)\sin(i_1) \\ a_1(\psi_2 - \psi_1) \end{bmatrix} \tag{2}$$

where the set $[a, e, i, \Omega, \omega, \psi]^\top \in \mathbb{R}^6$ represents the mean Keplerian elements vector; ψ indicates the mean argument of latitude to avoid singularities for nearly circular orbits. Within this context, the relative eccentricity and relative inclination are represented in vector form as follows:

$$a\Delta\boldsymbol{e} = a\begin{bmatrix}\Delta e_x \\ \Delta e_y\end{bmatrix} = a\delta e\begin{bmatrix}\cos(\phi) \\ \sin(\phi)\end{bmatrix} \tag{3}$$

$$a\Delta\boldsymbol{i} = a\begin{bmatrix}\Delta i_x \\ \Delta i_y\end{bmatrix} = a\delta i\begin{bmatrix}\cos(\theta) \\ \sin(\theta)\end{bmatrix} \tag{4}$$

where $a\delta e$ and $a\delta i$ represent the magnitudes of these vectors, while ϕ and θ denote their phases, referred to as the relative argument of perigee and the relative ascending node, respectively. These parameters describe the geometry of the relative orbit and define the points where the maximum vertical and horizontal distances occur. Starting from Eq. (2), it can be shown that the unperturbed relative motion can be broken down into the superposition of a harmonic oscillation perpendicular to the orbital plane and an elliptical in-plane motion, both governed by the magnitude and phase of the vectors $a\Delta\boldsymbol{e}$ and $a\Delta\boldsymbol{i}$. In addition, the radial and along-track separations exhibit systematic offsets and a linear drift due to Δa and $\Delta\psi$ [14]. The ideal Keplerian motion of the formation is disturbed by natural forces, leading to both periodic and long-term (secular) variations in the relative orbital elements. For formation-flying satellites, the short-period perturbations essentially cancel out [14], leaving only long-periodic and secular changes. For the GRACE-FO formation, the primary differential perturbations are caused by the Earth's asphericity and aerodynamic drag. A more detailed explanation can be found in [15] and [14], but in essence, Earth's asphericity causes the relative eccentricity vector to trace a clockwise circle with a radius of δe at the origin of the e-vector plane, with a period of approximately 100 days for sun-synchronous formations. The effect of aerodynamic drag is instead of particular interest for the GRACE-FO mission, as differential drag has been observed since the early phase of the satellites' orbital deployment, attributed to their differing ballistic coefficients. This discrepancy generates a relative along-track acceleration, which in turn causes an along-track offset, Δr_2, to accumulate over time according to the following equation:

$$\Delta r_2 = \frac{1}{2}\epsilon\,|\ddot{r}_D|\,\Delta t^2 \tag{5}$$

where $\epsilon \in \mathbb{R}_+$ represents the difference in the ballistic coefficients of the two spacecrafts, $|\ddot{r}_D| \in \mathbb{R}_+$ is the magnitude of the acceleration due to aerodynamic drag, and $\Delta t \in \mathbb{R}_+$ is a time interval of interest. Equation 5 defines the primary mechanism through which the manoeuvre control strategy maintains the formation within the along-track distance requirements of 220 ± 50 km, as further explained in Section 2.2. In general, to maintain the nominal formation configuration and to fulfill the objectives of the mission, the evolving relative elements are controlled by customized manoeuvres. Their direction and size can be computed using the simplified Gauss equations:

$$\begin{bmatrix} \delta\Delta a \\ a\delta\Delta e_x \\ a\delta\Delta e_y \\ a\delta\Delta i_x \\ a\delta\Delta i_y \\ a\delta\Delta\psi \end{bmatrix} = \frac{1}{n}\begin{bmatrix} 0 & 2 & 0 \\ \sin(\psi) & 2\cos(\psi) & 0 \\ -\cos(\psi) & 2\sin(\psi) & 0 \\ 0 & 0 & \cos(\psi) \\ 0 & 0 & \sin(\psi) \\ -2 & -3n(t - t_{\Delta v}) & \frac{-\sin(\psi)}{\tan(i)} \end{bmatrix}\begin{bmatrix} \Delta v_R \\ \Delta v_T \\ \Delta v_N \end{bmatrix} \tag{6}$$

Equation 6 illustrates the impact of a manoeuvre in the radial, along-track, cross-track (RTN) frame, with components $(\Delta v_R, \Delta v_T, \Delta v_N)$, on the changes $(\delta(*))$ in the rel-

ative orbital elements. These equations are generally valid for near-circular, non-equatorial orbits and applicable for GRACE-FO operations. It can be noted that the control problem is decoupled: an in-plane thrust $(\Delta v_R, \Delta v_T)$ affects the relative eccentricity vector, the relative semi-major axis, and the derivative of the relative argument of latitude. Conversely, an out-of-plane thrust (Δv_N) influences the relative inclination vector. In this work, we will focus solely on in-plane control, particularly on the effect of along-track manoeuvres, for several reasons: the formation control requirements concern only relative along-track and radial separation. In-plane control is typically executed through tangential manoeuvres due to their efficiency in terms of propellant consumption. Furthermore, CAMs are performed in the flight direction for the same reason. Out-of-plane manoeuvres, on the other hand, are only used to correct the inclination, and since GRACE-FO has no stringent requirements regarding Δi, they are not relevant to this context.

2.2 Manoeuvre Cycle

As mentioned before, the primary objective of the FD team is to maintain the formation within the along-track distance range of 220 ± 50 km to ensure the continuity of the LRI experiment. Recently, the science team at JPL requested that the inter-satellite distance be kept below 220 km, specifically between 170 and 220 km, since the onboard accelerometers were calibrated only for this range. While there is no indication that the accelerometers would not work outside this range, this adjustment was requested to match their calibration. To meet this requirement, the manoeuvre cycle has been designed to take advantage of the differential drag experienced by the satellites since the early stages of the mission. The formation is naturally decaying, but to maintain the correct along-track distance, manoeuvres are preferred to be performed using GF2. Figure 1 illustrates the natural drifting cycle of the GRACE-FO formation. Starting with an initial mean semi-major axis difference of 10 meters (shown on the right scale of the plot), the satellites gradually drift apart. Since GF2 experiences greater drag than GF1, its orbit decays more quickly, eventually reducing the relative semi-major axis difference to zero. At this point, the drift direction reverses, and the satellites begin to approach each other, reducing their relative along-track distance, as shown on the left scale of the plot. The three curves in blue, red, and green represent the nominal and $\pm 3 - \sigma$ predictions for formation monitoring, based on the current solar flux forecast. To maintain the formation, the manoeuvre cycle periodically raises GF2's orbit by approximately 20 meters, supporting the natural orbital decay. On average, this cycle lasts less than 90 days, depending on solar flux activity. Another key factor in maintaining the formation's science configuration is controlling the relative radial distance within a maximum threshold of ± 30 m. It can be shown that the factors affecting the radial range are the relative semi-major axis Δa and the magnitude of the eccentricity vector $a\Delta e$. When Δa is initialized to 10 meters, $a\Delta e$ is controlled to stay within an absolute value of approximately 20 meters. While eq. 6 suggest that, in theory, firing at specific values of u with a double pulse strategy could reduce the eccentricity vector to zero, this is not operationally achieved. In fact, to minimise the number of manoeuvre performed and thus the workload, FD team employs a single-pulse strategy, firing at a specific value of u to keep $a\Delta e$ constant in magnitude (within the required limits) and directed toward zero, as illustrated in figure 2.

2.3 Ground Activities Triggered by CAM Implementation

The described manoeuvre cycle can be interrupted by a conjunction event. GSOC FD team receives and monitors close-approach alerts in forms of Conjunction Data Messages (CDMs), which are generated by the 19th Space Defence Squadron (SDS) and relayed via NASA's Conjunction Analysis Risk Assessment (CARA) team. Each time a new Orbit Determination (OD) solution becomes available, GSOC FD sends an updated ephemeris to CARA. This last is then checked against the Special Perturbation catalogue, and if necessary, new CDMs are issued. These CDMs are retrieved and processed by the GSOC Collision Avoidance System (CAS) to assess their criticality. If a CAM is required, several ground activities are initiated. The science team is notified of the upcoming manoeuvre campaign, as the experiment temporarily needs to be paused. In fact, the LRI communication cannot be hold as the manoeuvre interrupts the formation relative pointing. The latest possible station passes for uploading the manoeuvre are identified. A key mission requirement is that there should be at least 2 upload opportunities (a prime and a back-up pass) before TCA and a pass shortly after execution to dump the relevant telemetry and have an indication of the correct performance. Once the prime upload time is defined, FD calculates the Δv and execution epoch, adjusting the burn duration to account for propulsion system rounding limitations. After preparing the manoeuvre, a new screening is conducted to reassess conjunction risks. The finalized manoeuvre is then uploaded during the agreed station pass. Following execution, GPS data is frequently dumped to calibrate the manoeuvre and estimate the post-manoeuvre orbit. This allows to perform an assessment on the formation status after the CAM and to plan a subsequent formation keeping manoeuvre to get back in science configuration.

3. Methodology

We consider a conjunction between a primary spacecraft, GF2, and a secondary object at a certain time $t_{CA} \in$

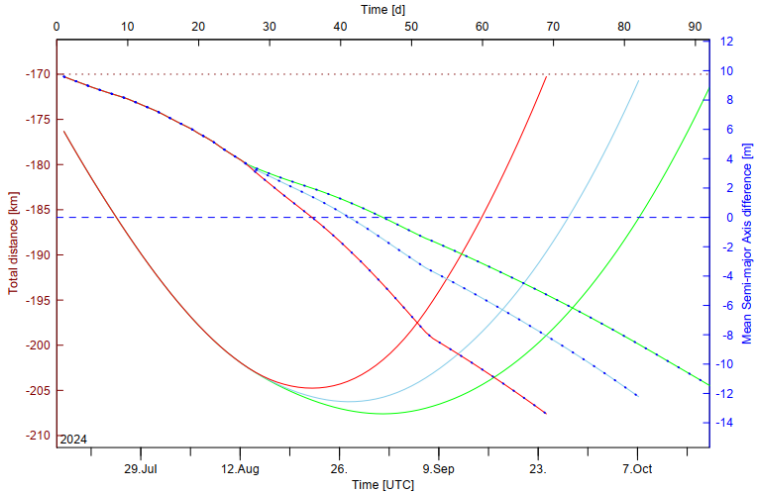

Fig. 1. GRACE-FO along-track distance (starting as red curve - left ordinate) and mean semi-major axis (blue dotted red curve - right ordinate)

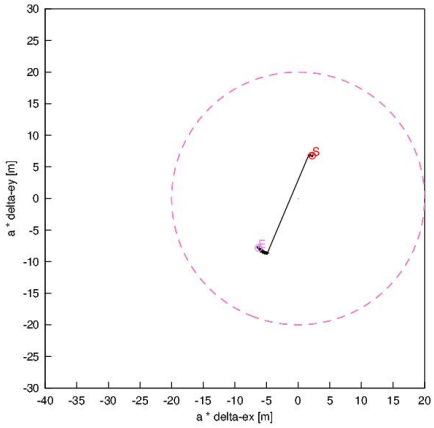

Fig. 2. Relative eccentricity vector control over one formation keeping cycle

$\mathbb{R}^2$. Primary and secondary states, respectively $\boldsymbol{x}_p(t_{CA})$ and $\boldsymbol{x}_s(t_{CA}) \in \mathbb{R}^6$, are Gaussian Multivariate Random Variables (MRVs) given by:

$$\boldsymbol{x}_p(t_{CA}) \sim \mathcal{N}(\boldsymbol{\zeta}_p(t_{CA}), \boldsymbol{C}_p(t_{CA})), \tag{7a}$$
$$\boldsymbol{x}_s(t_{CA}) \sim \mathcal{N}(\boldsymbol{\zeta}_s(t_{CA}), \boldsymbol{C}_s(t_{CA})) \tag{7b}$$

where, $\boldsymbol{\zeta}_p(t_{CA})$ and $\boldsymbol{\zeta}_s(t_{CA}) \in \mathbb{R}^6$ are the mean values, $\boldsymbol{C}_p(t_{CA})$ and $\boldsymbol{C}_s(t_{CA}) \in \mathbb{R}^{6\times6}$ are the covariance matrices expressed in a Cartesian space. $\boldsymbol{x}_p$ and $\boldsymbol{x}_s$ can be propagated employing Keplerian dynamics model as follows:

$$\dot{\boldsymbol{x}}_p(t) = \boldsymbol{f}(t, \boldsymbol{x}_p(t), \boldsymbol{u}(t)), \tag{8a}$$
$$\dot{\boldsymbol{x}}_s(t) = \boldsymbol{f}(t, \boldsymbol{x}_s(t), \boldsymbol{0}_3), \tag{8b}$$

where $t \in \mathbb{R}_{[t_0,t_f]}$ is the propagation time, belonging to an interval for which $t_0 < t_{CA} \leq t_f$. t represents the independent variable, while $\boldsymbol{x}_p(t), \boldsymbol{x}_s(t), \dot{\boldsymbol{x}}_p(t)$ and $\dot{\boldsymbol{x}}_s(t) \in \mathbb{R}^6$ are the time-dependent states of the primary and the secondaries and their derivatives. $\boldsymbol{u}(t) \in \mathbb{R}^3$ is the control action, and $\boldsymbol{f}(\cdot) : \mathbb{R}_{[t_0,t_f]} \times \mathbb{R}^6 \times \mathbb{R}^3 \to \mathbb{R}^6$ is the continuous Keplerian function. The relative position of the two objects is the subtraction of the first three elements of the two normally-distributed MRV:

$$\Delta\boldsymbol{r} = \boldsymbol{r}_p(t_{CA}) - \boldsymbol{r}_s(t_{CA}) \tag{9}$$

Since Eq. (9) is a linear transformation, $\Delta\boldsymbol{r}$ is also normally distributed:

$$\Delta\boldsymbol{r} \sim \mathcal{N}\left(\boldsymbol{\mu}_p - \boldsymbol{\mu}_s, \boldsymbol{P}_p + \boldsymbol{P}_s\right). \tag{10}$$

where the argument t_{CA} has been omitted because the metrics are only defined at TCA. The standard optimal control problem (OCP) in the continuous domain for the short-term conjunction CAM problem is stated as follows:

$$\min_{u} \quad J = \int_{t_0}^{t_f} u(t)\mathrm{d}t, \tag{11a}$$
$$\text{s.t.} \quad \dot{\boldsymbol{x}}_p = \boldsymbol{f}(t, \boldsymbol{x}_p(t), \boldsymbol{u}(t)), \tag{11b}$$
$$P_C(t) \leq \bar{P}_C, \tag{11c}$$
$$\boldsymbol{x}(t_0) = \boldsymbol{x}_0, \tag{11d}$$
$$u(t) = \sqrt{u_1(t)^2 + u_2(t)^2 + u_3(t)^2}, \tag{11e}$$
$$u(t) \leq u_{max}, \tag{11f}$$

where $P_C \in \mathbb{R}_+$ represents the PoC, and $\bar{P}_C \in \mathbb{R}_+$ is its maximum allowed limit value. In Problem (11), Eq. (11a) represents the fuel minimization objective function, Eq. (11b) is the dynamics constraint, Eq. (11c) is the PoC constraint, Eq. (11d) is the initial state bound, Eq. (11e) is an auxiliary constraint to define the norm of the control, and Eq. (11f) is the bound on the maximum value of the control action. Since CAMs typically involve a Δv on the order of magnitude of $[\mathrm{mm/s}]$ or $[\mathrm{cm/s}]$, the mass loss due to the manoeuvre is not considered in the equations of motion and in the optimisation problem [8].

3.1 Encounter Dynamics

During short-term conjunctions, the high relative velocity leads to near-instantaneous encounters [16]. As a result, the path of relative motion can be effectively approximated as linear, and the event is typically analyzed on the two-dimensional B-plane [8, 17–19]. This reference frame is centred on the secondary object, and it is defined as the plane perpendicular to the relative velocity vector. Since TCA, by definition, is the time when the miss distance is lowest, it follows that $\Delta\boldsymbol{r}_s(t_{CA}) \cdot \Delta\boldsymbol{v}_s(t_{CA}) = 0$ and thus the relative position lies on the B-

plane. As outlined in [17, 20], the problem is traditionally studied by centring the combined positional uncertainty of both objects $\boldsymbol{P}_{comb}(t_{CA})$ around the secondary object, while a sphere of radius $HBR = HBR_s + HBR_p$, embodying both objects dimensions, is centred around the primary. This allows the primary's state, which needs to be optimised, to be treated as a deterministic variable. In this framework, the PoC can be computed by integrating the (PDF) of the relative position over the projection of the combined sphere $\mathbb{C}_{\text{HBR}}$ onto the B-plane.

$$P_C = \frac{1}{(2\pi)\sqrt{\det\left(\boldsymbol{P}_{\mathcal{B}}(t_{CA})\right)}} \cdot \cdot \iint_{\mathbb{C}_{\text{HBR}}} \exp\left(-\frac{\Delta \boldsymbol{r}_{\mathcal{B}}^{\top} \boldsymbol{P}_{\mathcal{B}}^{-1} \Delta \boldsymbol{r}_{\mathcal{B}}}{2}\right) \mathrm{d}A, \tag{12}$$

where $\Delta \boldsymbol{r}_{\mathcal{B}} \in \mathbb{R}^2$ and $\boldsymbol{P}_{\mathcal{B}} \in \mathbb{R}^{2\times 2}$ are respectively the projection of the relative position mean value and covariance on the encounter B-plane at TCA. The argument of the exponential function is the SMD at TCA, $d_m^2 \in \mathbb{R}_+$, divided by 2. Various approaches have been proposed to numerically solve this integral over the years; in this work, we will use Chan's method [21], which is generally preferred over others because of its accuracy and computational efficiency [22]. By employing a numerical inversion of Chan's formula [19], it is possible to get the SMD limit from a PoC limit for the conjunction ($\bar{d}_m^2 = f(\bar{P}_C)$).

3.2 Convex Formulation

The OCP Problem 11 is converted into a sequential convex program (SCP), following the methods outlined in [3–5]. The SCP iteratively approximates the global solution of the OCP using a series of second-order cone programs (SOCPs). Here, we briefly summarize the constraints and objective function. The original OCP in Problem 11 contains three sources of non-convexity:

1. The orbital dynamics in Eq. (11b) are nonlinear and thus non-convex.
2. The constraint in Eq. (11c) is nonlinear due to Eq. (12) and the inversion of Chan's formula.
3. Both Eq. (11a) and Eq. (11e) produce a nonlinear objective function.

In the following subsections, the dynamics constraint, the PoC constraint, and the objective function are convexified using different techniques. Detailed explanations of these methods can be found in [3, 5].

3.2.1 Convexification of the Dynamics

The dynamics of the problem are first discretized and then linearized using DA. In the following discussion, the continuous time variable $t \in \mathbb{R}_{[t_0,t_f]}$ is substituted by the discrete time variable $t_i \in \{t_0, t_1, ..., t_N\}$, where $N+1$ is the number of nodes of the discretization. The equations that present the index i are valid for all $i \in \{0, \dots, N\}$. An ephemeris-based propagation approach is selected to enhance the algorithm's operational value. As a result, the nominal trajectory is defined by the vectors $\boldsymbol{x}_i^{eph}$, which are derived from the operator's direct high-fidelity orbit determination. At any iteration $j > 1$, the output state and control from the previous iteration are used to build the dynamics continuity constraint. A first-order Taylor polynomial expanding the dynamics function in Eq. (14) around this reference, which is denoted by $\tilde{\boldsymbol{x}}_i \in \mathbb{R}^6$, $\tilde{\boldsymbol{u}}_i \in \mathbb{R}^3$; the reference trajectory is selected as $\boldsymbol{x}_i^{eph}$ in the first iteration. The states and control are expanded as

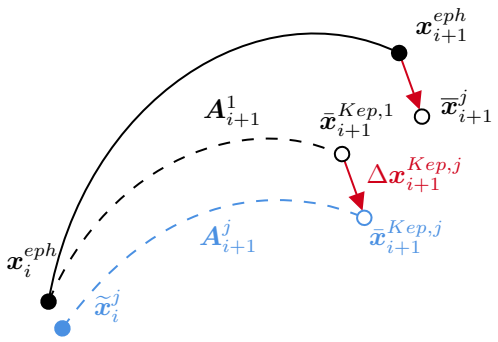

Fig. 3. Schematics of the dynamics constraints within the ephemeris propagation framework.

$$\boldsymbol{x}_i^j = \tilde{\boldsymbol{x}}_i^j + \delta \boldsymbol{x}_i \tag{13a}$$

$$\boldsymbol{u}_i^j = \tilde{\boldsymbol{u}}_i^j + \delta \boldsymbol{u}_i \tag{13b}$$

Using DA and an Runge-Kutta integrationg scheme, the state of the primary at node $i+1$ can be determined based on the reference state of the previous node, $\tilde{\boldsymbol{x}}_i^j$, using the Keplerian model:

$$\boldsymbol{x}_{i+1}^{Kep,j} = \mathcal{T}_{\boldsymbol{x}_i}(\tilde{\boldsymbol{x}}_i^j + \delta \boldsymbol{x}_i, \tilde{\boldsymbol{u}}_i^j + \delta \boldsymbol{u}_i) \tag{14}$$

where $\mathcal{T}_{\boldsymbol{x}_i}(\cdot) : \mathbb{R}^6 \times \mathbb{R}^3 \to \mathbb{R}^6$ is the Taylor expansion of the Keplerian dynamics, $\boldsymbol{x}_i = \boldsymbol{x}(t_i)$, and $\boldsymbol{u}_i = \boldsymbol{u}(t_i)$. The left-hand member of Eq. (14) can be split into a constant part and a linear part:

$$\boldsymbol{x}_{i+1}^{Kep,j} = \bar{\boldsymbol{x}}_{i+1}^{Kep,j} + \delta \boldsymbol{x}_{i+1}^{Kep,j}. \tag{15}$$

Both terms of the right-hand side of Eq. (15) can be expressed as follows:

$$\bar{\boldsymbol{x}}_{i+1}^{Kep,j} = \boldsymbol{f}_i(\tilde{\boldsymbol{x}}_i^j, \tilde{\boldsymbol{u}}_i^j), \tag{16a}$$

$$\delta \boldsymbol{x}_{i+1}^{Kep,j} = \boldsymbol{A}_{i+1}^j \delta \boldsymbol{x}_i + \boldsymbol{B}_{i+1}^j \delta \boldsymbol{u}_i, \tag{16b}$$

where $\boldsymbol{f}_i(\cdot) : \mathbb{R}^6 \times \mathbb{R}^3 \to \mathbb{R}^6$ is the discretized version of Eq. (8), $\boldsymbol{A}_{i+1}^j \in \mathbb{R}^6$ and $\boldsymbol{B}_{i+1}^j \in \mathbb{R}^6$ are the Keplerian state transition and control-state transition matrices, respectively, automatically derived using DA. To ensure fidelity to the ephemeris, information from the nominal trajectory is incorporated at each iteration. Specifically,

at iteration j, a segmented Keplerian propagation is performed starting from the optimisation output of the previous iteration $(j-1)$ or from the nominal ephemeris if $j=1$, as described in Eq. (14). The linear deviation between the constant part of the Keplerian-propagated trajectory at iteration j and the initial trajectory is then evaluated as:

$$\Delta \boldsymbol{x}_{i+1}^{Kep,j} = \bar{\boldsymbol{x}}_{i+1}^{Kep,j} - \bar{\boldsymbol{x}}_{i+1}^{Kep,1}. \tag{17}$$

where $\Delta \boldsymbol{x}_{i+1}^{Kep,j}$ is used to linearly correct the nominal ephemeris to account for the effect of the computed control at iteration j. Thus, the constant part of the propagation that is used to define the dynamics continuity constraint is

$$\bar{\boldsymbol{x}}_{i+1}^{j} = \boldsymbol{x}_{i+1}^{eph} + \Delta \boldsymbol{x}_{i+1}^{Kep,j}. \tag{18}$$

This method allows for maintaining high-fidelity propagation while generating sufficiently accurate linear Keplerian maps to describe the node-wise evolution of the trajectory, as shown in Fig. 3. It's important to note that this approach would become inaccurate if large deviations from the nominal trajectory were expected. However, based on CAM optimisation theory, it is reasonable to assume that deviations are on the order of kilometers, since the manoeuvres are in the range of centimeters per second. As a result, these deviations are almost negligible on an orbital scale. The continuity constraint of the SOCP is therefore defined by equating Eq. (13) and Eq. (15):

$$\boldsymbol{x}_{i+1}^{j,k} = \boldsymbol{A}_{i+1}^{j} \boldsymbol{x}_{i}^{j,k} + \boldsymbol{B}_{i+1}^{j} \boldsymbol{u}_{i}^{j,k} + \boldsymbol{c}_{i+1}^{j} \tag{19}$$

where $\boldsymbol{c}_{i+1} = \bar{\boldsymbol{x}}_{i+1}^{j} - \boldsymbol{A}_{i+1}^{j} \tilde{\boldsymbol{x}}_{i}^{j} - \boldsymbol{B}_{i+1}^{j} \tilde{\boldsymbol{u}}_{i}^{j}$ is the residual of the linearization corrected for the ephemeris propagation.[1] This is an iterative process referred to as major iterations and denoted by index j. Once the optimisation problem of a major iteration j is solved, the solution ($\boldsymbol{x}_i^j$, $\boldsymbol{u}_i^j$, for $i \in \{0, \dots, N-1\}$) becomes available and is used as an expansion point for constructing $\boldsymbol{A}_{i+1}^{j+1}$ and $\boldsymbol{B}_{i+1}^{j+1}$, and $\boldsymbol{c}_{i+1}^{j+1}$, as described in the previous paragraph. The initial condition is fixed because the manoeuvre cannot alter it

$$\boldsymbol{x}_{0}^{j,k} = \boldsymbol{x}_{0}^{eph}. \tag{20}$$

3.2.2 Lossless Relaxation of the Control Magnitude Constraint

Equation Eq. (11e) is a non-convex equality constraint. Following [6], we introduce a lossless relaxation to convexify the constraint: Eq. (11e) is transformed into an inequality constraint, and the control magnitude is added to the optimisation vector. In this way, Eq. (11e) becomes a second-order cone constraint. The variable u_i is now allowed to take values higher than the norm of the control that acts on the dynamics

$$u_i \geq \sqrt{u_{i,r}^2 + u_{i,t}^2 + u_{i,n}^2} \tag{21}$$

The discretized forms of Eq. (11a) and Eq. (11f) become respectively

$$J = \sum_{i=0}^{N-1} u_i \cdot \Delta t_i, \tag{22}$$

with

$$0 \leq u_i \leq 1, \tag{23}$$

where $\Delta t_i = t_{i+1} - t_i$ is the time for which the control is active from node i to $i+1$. This linearization of the objective function is lossless, meaning that the optimal solution for the convexified problem is also optimal for the original problem.

3.2.3 Trust Region Approach

Using a trust region constraint in the formulation of the SOCP significantly improves the algorithm's convergence [23]. This approach, first introduced in [24] and adapted in [3], builds on the definition of the nonlinearity index (NLI) from [25].For detailed information on the derivation of the constraint, readers are encouraged to consult these sources. In essence, the approach treats the trust region radius of an optimisation variable as inversely proportional to its non-linearity. The resulting constraints are:

$$\boldsymbol{\xi}_i \circ [\boldsymbol{x}_i^\top;\, \boldsymbol{u}_i^\top]^\top \preceq \boldsymbol{\xi}_i \circ [\tilde{\boldsymbol{x}}_i^\top;\, \tilde{\boldsymbol{u}}_i^\top]^\top + \bar{\nu} \cdot \mathbf{1}, \tag{24a}$$

$$\boldsymbol{\xi}_i \circ [\boldsymbol{x}_i^\top;\, \boldsymbol{u}_i^\top]^\top \succeq \boldsymbol{\xi}_i \circ [\tilde{\boldsymbol{x}}_i^\top;\, \tilde{\boldsymbol{u}}_i^\top]^\top - \bar{\nu} \cdot \mathbf{1}, \tag{24b}$$

where $\boldsymbol{\xi}_i$ is the measure of non-linearity of the associated state vector in the second-order DA propagation of the dynamics [24]; $\bar{\nu}$ is a user-defined value that imposes a limit to the maximum NLI available to the solution.

The introduction of the trust region constraint can cause artificial infeasibility, so virtual controls are added to the dynamics constraints, Eq. (19). The new constraints with virtual controls become

$$\boldsymbol{x}_{i+1}^{j} - \boldsymbol{A}_{i+1} \boldsymbol{x}_{i}^{j} - \boldsymbol{B}_{i+1}^{j} \boldsymbol{u}_{i}^{j} + \boldsymbol{v}_{i+1}^{j} - \boldsymbol{c}_{i}^{j} = 0 \tag{25}$$

where $\boldsymbol{v}_i^j \in \mathbb{R}^6$ is the virtual control vector for the node i at major iteration j.

A term proportional to the magnitude of the virtual controls is added to the objective function to minimize their impact. This term is scaled by a weight factor $\kappa_{vc} \in \mathbb{R}$, which must be set sufficiently high.

$$\upsilon_i \geq ||(\upsilon_{ca,i}^j)||, \tag{26a}$$

$$J_{vc} = \kappa_{vc} \sum_{i=0}^{N} \upsilon_i, \tag{26b}$$

[1] In Eq. (19), the index k has been used to address the minor iterations which are described in Section 3.2.4.

3.2.4 Linearized SMD Constraint

The PoC constraint for a single conjunction can be formulated by leveraging the methodology proposed in references [26] and [8]. The reader is invited to refer to this last reference for an in-depth explanation of the process. An iterative projection and linearization algorithm is utilized to convexify the non-linear PoC constraint. The iterations are nested inside the major iterations (used to linearize the dynamics) and take the name of *minor iterations*, denoted by the symbol k. For each conjunction node, the projected convex sub-problem aims to find the point on the surface of an ellipse that is closest to the relative position $\Delta \boldsymbol{r}^{j,k-1}$ from the previous minor iteration. In the formulation of the convex sub-problem, the index j is dropped since one of these problems is solved multiple times inside the same major iteration.

Let the covariance and relative position be expressed in the B-plane reference frame $\mathcal{B}$. It is possible to define a transformation matrix $\boldsymbol{V} \in \mathbb{R}^2$ that diagonalizes the covariance matrix. We call the reference frame in which the covariance matrix is diagonal $\mathcal{C}$. A simple quadratic optimisation problem is used to find the point on the ellipse that is closest to the reference trajectory point

$$\min_{\hat{\boldsymbol{z}}_{\mathcal{C}}} \quad ||\boldsymbol{z}_{\mathcal{C}}^{k} - \Delta \boldsymbol{r}_{q,\mathcal{C}}^{k-1}|| \tag{27a}$$

$$\text{s.t.} \quad (\boldsymbol{z}_{\mathcal{C}}^{k})^{\top} (\boldsymbol{P}_{\mathcal{C}})^{-1} \boldsymbol{z}_{\mathcal{C}}^{k} \leq \bar{d}_m^2, \tag{27b}$$

The objective Eq. (27a) imposes the minimization of the Euclidean distance between the relative position of the previous iteration and the optimisation variable $\boldsymbol{z}_{\mathcal{C}}$. Eq. (27b) is a relaxed condition on the optimisation variable to be inside the ellipsoid. These relaxed conditions are lossless since the minimization of the objective guarantees that the optimised variable is always positioned on the ellipse's surface, maximizing the distance from its center.

Once $\boldsymbol{z}_{\mathcal{C}}$ is determined, the solution is transformed back into the original reference frame using the equation $\boldsymbol{z}_{\mathcal{B}}^{k} = \boldsymbol{V}^{\top} \boldsymbol{z}_{\mathcal{C}}^{k}$. After obtaining $\boldsymbol{z}^{j,k} = \boldsymbol{z}_{\mathcal{B}}^{k}$, a linearization of the SMD constraint is applied, effectively turning it into a keep-out zone (KOZ) constraint. Specifically, we ensure that the new optimised relative position lies within the semi-plane defined by the line tangent to the ellipse on $\boldsymbol{z}_s^{j,k}$. The equation of the constraint is, then

$$\nabla (d_m^2)^{j,k} \Big|_{\boldsymbol{z}^{j,k}} \cdot (\Delta \boldsymbol{r}^{j,k} - \boldsymbol{z}^{j,k}) \geq 0. \tag{28}$$

The base CAM optimisation problem, before the inclusion of operational constraints, can thus be written as

$$\min_{\boldsymbol{u},\boldsymbol{x},\boldsymbol{\nu}} \quad \sum_{i=1}^{N} (\Delta t_i u_i + \kappa_{vc} \upsilon_i) \tag{29}$$

$$\text{s.t.} \quad \text{Eqs. (19) to (21), (23), (24), (26a) and (28)}$$

3.3 Operational Constraints

In this subsection, the mission constraints are integrated into the CAM optimisation problem, following the formation control logic outlined in Section 2.

3.3.1 Relative Orbital Elements

To control the long-term evolution of the formation, Δa and $a\Delta e$ are controlled at the end of the window of interest. Consider the transformation between the Cartesian state of the two satellites and their relative mean Keplerian orbital elements in Eq. (1). The first three elements of this transformation yield, respectively, the mean semi-major axis difference and the two components of the mean relative eccentricity vector. Calling the state of GF1 $\boldsymbol{x}_{ref,i}$ Let us expand this transformation with respect to the state of GF2 at the final time:

$$\begin{bmatrix} \Delta a \\ a1\Delta e_x \\ a1\Delta e_y \end{bmatrix} = \begin{bmatrix} g_1(\boldsymbol{x}_{ref,N}, \tilde{\boldsymbol{x}}_N^j + \delta \boldsymbol{x}) \\ g_2(\boldsymbol{x}_{ref,N}, \tilde{\boldsymbol{x}}_N^j + \delta \boldsymbol{x}) \\ g_3(\boldsymbol{x}_{ref,N}, \tilde{\boldsymbol{x}}_N^j + \delta \boldsymbol{x}) \end{bmatrix}, \tag{30}$$

where g_1, g_2 and $g_3 : \mathbb{R}^6 \times \mathbb{R}^6 \to \mathbb{R}$ are the first three components of the transformation, and $\tilde{\boldsymbol{x}}_N^j \in \mathbb{R}^6$ is the reference state from the output of the optimiser at the previous iteration. The first order expansion yields a linear map for the relative semi-major axis, $\boldsymbol{l} \in \mathbb{R}^6$, and one for the relative eccentricity vector, $\boldsymbol{L} \in \mathbb{R}^{2\times 6}$.

The relative semi-major axis should be inside a tight band of amplitude $2b$ (20 m). So, the equation of the constraint is

$$-b \leq \Delta a \leq b. \tag{31}$$

Let us link perturbations in the final state to perturbations in a_{rel}, via the first-order DA expansion

$$\delta \Delta a = \boldsymbol{l}^j \cdot \delta \boldsymbol{x}_N^{j,k}. \tag{32}$$

After a trivial procedure similar to the one shown for Eq. (19), the final equation of the constraint becomes

$$\boldsymbol{l}^j \cdot \boldsymbol{x}_N^{j,k} \leq \boldsymbol{l}^j \cdot \tilde{\boldsymbol{x}}_N^j - \Delta \bar{a} + b \tag{33a}$$

$$\boldsymbol{l}^j \cdot \boldsymbol{x}_N^{j,k} \geq \boldsymbol{l}^j \cdot \tilde{\boldsymbol{x}}_N^j - \Delta \bar{a} - b \tag{33b}$$

where $\Delta \bar{a}$ is the constant part of the first element of Eq. (30), and $\tilde{\boldsymbol{x}}_N^j$ is the expansion point of the optimisation.

The relative mean eccentricity vector is controlled in a similar way, with the only difference that a target relative eccentricity vector is selected based on the strategy presented in Section 2. Therefore, we want to target the opposite point on the eccentricity plane

$$\boldsymbol{e}_{rel} = -\boldsymbol{e}_{rel}^0, \tag{34}$$

where $\boldsymbol{e}_{rel}^0 \in \mathbb{R}^2$ is the relative eccentricity vector of the unperturbed trajectory (ephemeris). Using the linear maps as before, the requirement of Eq. (34) becomes

$$\boldsymbol{L}^j \boldsymbol{x}_N^{j,k} = \boldsymbol{L}^j \tilde{\boldsymbol{x}}_N^j - \bar{\boldsymbol{e}}_{rel} - \boldsymbol{e}_{rel}^0, \tag{35}$$

where $\bar{\boldsymbol{e}}_{rel}$ is the constant part of the last two elements of Eq. (30).

3.3.2 Relative Altitude and Maximum Formation Altitude

We want to enforce two constraints on the altitude of GF2. To simplify the polynomial expansion and ensure the relative value remains positive, we express these constraints using the squared altitude of the spacecraft, avoiding the need for square roots. Let $\boldsymbol{r}_N^{j,k} \in \mathbb{R}^3$ denote the Earth Centered Inertial (ECI) position of the final state at iterations j and k (the first three elements of the state vector). The absolute altitude constraint, expressed in terms of orbital radius, is given by

$$r_{lo}^2 < ||\boldsymbol{r}_N^{j,k}||^2 < r_{up}^2, \tag{36}$$

where r_{lo} and $r_{up} \in \mathbb{R}_+$ are the lower and upper limits, respectively. The perturbed final position can be written as $\boldsymbol{r}_N^{j,k} = \tilde{\boldsymbol{r}}_N^j + \delta\boldsymbol{r}$, where $\tilde{\boldsymbol{r}}_N^j$ is the expansion point from the previous major iteration (first three elements of $\tilde{\boldsymbol{x}}_N^j$). The polynomial expansion of the squared radius, then, can be written as,

$$||\boldsymbol{r}_N^{j,k}||^2 = ||\tilde{\boldsymbol{r}}_N^j||^2 + 2\tilde{\boldsymbol{r}}_N^j \cdot \delta\boldsymbol{r}_N \tag{37}$$

Substituting the absolute altitude requirement becomes the convex constraint

$$2\tilde{\boldsymbol{r}}_N^j \cdot \boldsymbol{x}_N^{j,k} \leq 2\tilde{\boldsymbol{r}}_N^j \cdot \tilde{\boldsymbol{r}}_N^j - ||\tilde{\boldsymbol{r}}_N^j||^2 + h_{up}^2 \tag{38a}$$

$$2\tilde{\boldsymbol{r}}_N^j \cdot \boldsymbol{x}_N^{j,k} \geq 2\tilde{\boldsymbol{r}}_N^j \cdot \tilde{\boldsymbol{r}}_N^j - ||\tilde{\boldsymbol{r}}_N^j||^2 + h_{lo}^2 \tag{38b}$$

The requirement regarding the relative altitude between the two satellites is automatically satisfied when the constraints on the relative orbital elements are respected.

3.3.3 Relative Distance

At the end of the CAM, GF2 must stay inside the tangential separation bounds reported in Section 2

$$b_{lo} \leq \Delta r_t \leq b_{up}. \tag{39}$$

where $\Delta r_t \in \mathbb{R}$ is the tangential separation, and b_{lo} and $b_{up} \in \mathbb{R}$ are the lower and upper bounds, respectively. Let us call $\boldsymbol{R}$ the rotation matrix between the ECI reference frame used for the propagation, $\mathcal{E}$, and the RTN orbital frame of GF1, $\mathcal{O}$. By definition, the position of GF1 in this frame is $\boldsymbol{r}_{\mathcal{O},1} = [||\boldsymbol{r}_{\mathcal{E},1}||_2,\ 0,\ 0]^\top$. The relative position of GF2 is, therefore

$$\Delta\boldsymbol{r}_{\mathcal{O}} = \boldsymbol{r}_{\mathcal{O},2} - \boldsymbol{r}_{\mathcal{O},1} = \boldsymbol{R}\boldsymbol{r}_{\mathcal{E},2} - \boldsymbol{r}_{\mathcal{O},1}. \tag{40}$$

If we call $\boldsymbol{R}_2 \in \mathbb{R}^3$ the second row of $\boldsymbol{R}$, the tangential separation becomes

$$\Delta T = \boldsymbol{R}_2\boldsymbol{r}_{\mathcal{E},2}. \tag{41}$$

Eq. (41) can be used to set a final constraint in terms of tangential separation. Referring to a generic major iteration j and minor iteration k, the final separation distance constraint becomes

$$b_{lo} \leq \boldsymbol{R}_2 \cdot \boldsymbol{r}_N^{j,k} \leq b_{up}, \tag{42}$$

where, once again, $\boldsymbol{r}_N^{j,k} \in \mathbb{R}^3$ is made up by the first three elements of $\boldsymbol{x}_N^{j,k}$.

The final optimisation problem, with all the operational constraints, is expressed as

$$\begin{aligned} \min_{\boldsymbol{u},\boldsymbol{x},\boldsymbol{\nu}} \quad & \sum_{i=1}^{N}(\Delta t_i u_i + \kappa_{vc}\upsilon_i) \\ \text{s.t.} \quad & \text{Eqs. (19), (21), (23), (24), (26a) and (28)} \\ & \text{Eqs. (20), (33), (35), (38) and (42)} \end{aligned} \tag{43}$$

3.3.4 Tangential Thrust

As explained in 2.1, except in special operational scenarios, in-plane control is achieved solely through tangential manoeuvres. This constraint can be implemented into the optimiser by forcing the radial and normal components of the control to always be zero. Doing so simplifies the problem significantly, as the second-order cone constraint on the control becomes unnecessary:

$$\begin{aligned} \min_{\boldsymbol{u},\boldsymbol{x},\boldsymbol{\nu}} \quad & \sum_{i=1}^{N}\Big(\Delta t_i(u_{T,i}^+ - u_{T,i}^-) + \kappa_{vc}\upsilon_i\Big) \\ \text{s.t.} \quad & \text{Eqs. (19), (24), (26a) and (28)} \\ & \text{Eqs. (20), (33), (35), (38) and (42)} \\ & \boldsymbol{u}_i = [0,\ u_{T,i}^+ - u_{T,i}^-,\ 0]^\top \\ & 0 \leq u_{T,i}^+, u_{T,i}^- \leq u_{max}, \end{aligned} \tag{44}$$

where $u_{T,i}^+$ and $u_{T,i}^- \in \mathbb{R}_+$ are the positive and negative components of the tangential thrust of node i, respectively.

4. Real Test-Case Conjunctions Operations

For the following test cases, the maximum control acceleration is conservatively set to $u_{max} = 0.18\ \mathrm{mm/s^2}$, consistent with the largest manoeuvres performed by the GRACE-FO operations team. The orbit is uniformly discretized with a time step of $\Delta t = 60$ s, meaning the optimiser can produce a maximum single Δv per time step of:

$$\Delta v_{max} = u_{max}\Delta t = 10.8\ \mathrm{mm/s}$$

Convergence on the major iterations is reached when the virtual control all almost 0, i.e., $\sum_{i=0}^{N}\upsilon_i < 10^{-14}$ and the parameter $\epsilon \in \mathbb{R}_+$ is below a threshold, set to 10^{-4}: this parameter is defined as

$$\epsilon = \sum_{i=0}^{N-1} ||\boldsymbol{u}_i^j - \boldsymbol{u}_i^{j-1}||_2. \tag{45}$$

4.1 Single Encounter

Let us first consider an operational case in which GF2 undergoes a close encounter with an uncontrolled payload. The states in True of Date (ToD) of the two objects

at TCA epoch 2024-01-04 16:51:39.162 UTC are:

$$\boldsymbol{r}_{p,CA} = [-3718.784, \quad 3046.446, \quad 4898.430]^\top \text{km},$$
$$\boldsymbol{v}_{p,CA} = [-4.335022, \quad 3.302274, \quad -5.322456]^\top \text{km/s}.$$
$$\boldsymbol{r}_{s,CA} = [-3718.780, \quad 3046.434, \quad 4898.419]^\top \text{km},$$
$$\boldsymbol{v}_{s,CA} = [5.045387, \quad -2.27021, \quad 5.239002]^\top \text{km/s}.$$

With respective positional covariance matrices as:

$$\boldsymbol{P}_p = \begin{bmatrix} 64.8812 & 0.0 & 0.0 \\ 0.0 & 470939.6 & 0.0 \\ 0.0 & 0.0 & 36.36978 \end{bmatrix} \text{m}^2$$

$$\boldsymbol{P}_s = \begin{bmatrix} 584.5167 & -32943.42 & -22.66674 \\ -32943.42 & 2212296 & -332.5021 \\ -22.66674 & -332.5021 & 76.23035 \end{bmatrix} \text{m}^2.$$

These data result in a miss distance of 16.4 m and a PoC of 3.95×10^{-4}, using Chan's method with an HBR of 1.7 m. The manoeuvre is computed to reduce PoC below 10^{-6}. As discussed above, when monitoring a close approach, operators typically tend to wait for the final CAM GO/NO-GO decision, hoping that updated orbit assessments will reduce the severity of the event. If the situation remains critical, a CAM is executed, followed by an *a posteriori* formation-keeping manoeuvre after the conjunction. In this scenario, the analysis begins two hours before TCA and includes an additional two hours for the formation-keeping manoeuvres. The behaviour of the optimiser, in the first instance, is assessed considering only the CAM. In this case, the optimiser finds a single firing spread over two nodes exactly 0.5 orbits before the conjunction: the RTN components of the Δv are

$$\Delta v = [-0.036, \ 10.511, \ -0.010]^\top \text{mm/s}.$$

It is clear from the literature [8, 19, 27] that this is to be expected in a simple scenario like this since a tangential firing half-an-orbit before TCA maximises the deviation in the B-plane. The B-plane configuration can be seen in Fig. 4. It is worth noting that employing the formulation in Eq. (44) is very beneficial when the simple single short-term encounter problem is addressed. Indeed, the optimiser finds almost the same solution, free of the irrelevant R and N components, increasing the T components by just 1 μm/s:

$$\Delta v = [0, \ 10.512, \ 0]^\top \text{mm/s}.$$

Including the formation-keeping (FK) constraints detailed in Problem (43) yields the thrust profile in Fig. 7. The first impulse is shifted back by one node compared to the case with no FK requirements, but it is essentially the same manoeuvre. As can be seen in Fig. 7, the FK conditions are fulfilled by the two consecutive manoeuvres, one performed at TCA and the second 0.5 orbits after. The total Δv grows up to 3.9 cm/s, and it is still

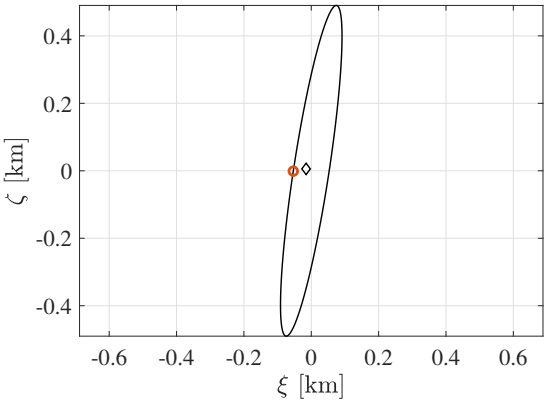

Fig. 4. B-plane of the first conjunction. diamond: ballistic, red dot: manoeuvred

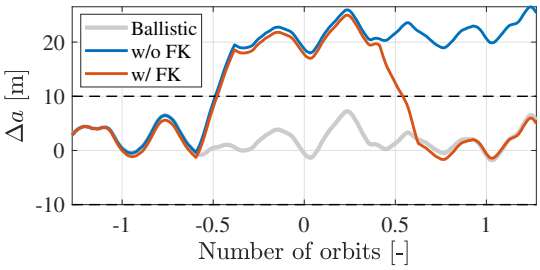

Fig. 5. Evolution of the mean relative semi-major axis in the single conjunction scenario.

mostly tangential, as expected from the theory in Section 2. In particular,Figs. 5 and 6 show that, while the manoeuvre with no FK requirements violates the mean relative semi-major axis and mean relative eccentricity vector constraints, their inclusion allows us to target the required conditions very accurately.

4.2 Multiple Encounters

As a second test case, we are presenting an interesting operational scenario involving two consecutive conjunctions that took place in January 2024. The first conjunction studied in the previous section is followed by a second one two days later. As expected, the uncertainty at the second TCA for both objects is higher than at the first due to the increased propagation error in the OD solution at the time of analysis. Despite this, it is valuable to assess the effect of the optimiser's computed CAM on both conjunctions. The predicted states of GF2 and the secondary

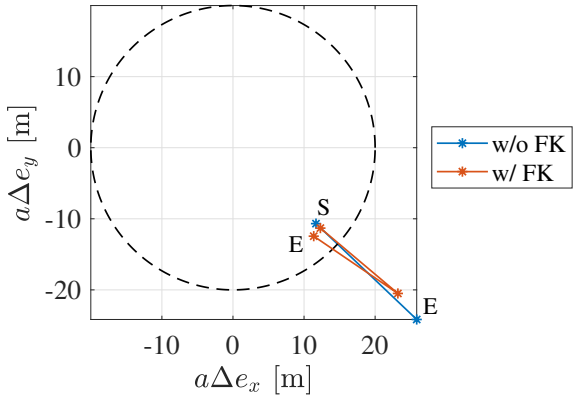

Fig. 6. Evolution of the mean relative eccentricity vector in the single conjunction scenario.

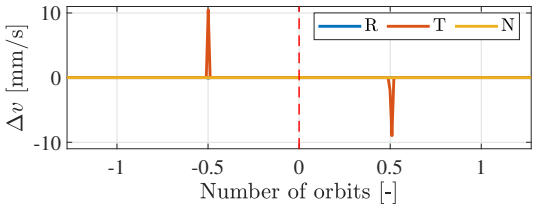

Fig. 7. Δv for the optimised CAM with FK constraints.

object at TCA epoch 2024-01-06 11:27:48.122 UTC are:

$$\boldsymbol{r}_{p,CA2} = [-4892.212, \quad -4690.717, \quad 1130.894]^\top \text{km},$$
$$\boldsymbol{v}_{p,CA2} = [-1.158113, \quad -0.615334, \quad -7.507123]^\top \text{km/s},$$
$$\boldsymbol{r}_{s,CA2} = [-4891.089, \quad -4692.144, \quad 1129.967]^\top \text{km},$$
$$\boldsymbol{v}_{s,CA2} = [4.544310, \quad -3.725686, \quad 4.188866]^\top \text{km/s}.$$

The positional covariances of the two objects are

$$\boldsymbol{P}_{p2} = \begin{bmatrix} 212.117 & 0.0 & 0.0 \\ 0.0 & 5770985 & 0.0 \\ 0.0 & 0.0 & 74.174 \end{bmatrix} \text{m}^2$$

$$\boldsymbol{P}_{s2} = \begin{bmatrix} 3284.89 & -366714.4 & -52.3355 \\ -366714.4 & 49998130 & 41402.66 \\ -52.3355 & 41402.66 & 254.2109 \end{bmatrix} \text{m}^2.$$

These data result in a miss distance of 2.039 km and a PoC of 3.6×10^{-4}, using Chan's method with an HBR of 1.7 m. The manoeuvre is computed to reduce total probability of collision (TPoC) below 10^{-6}, so the effect of both conjunctions is combined to achieve a desired comprehensive collision risk. In this case, the testing scenario is bound to start 3 hours before the first TCA and end 2 hours and 24 min after the second one. Once again, the scenario is initially tested without applying the formation-keeping constraint. In this case, the optimiser computes two manoeuvres before the TCA. The first manoeuvre

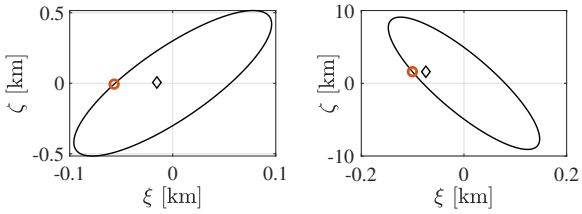

Fig. 8. B-plane of the two conjunctions.

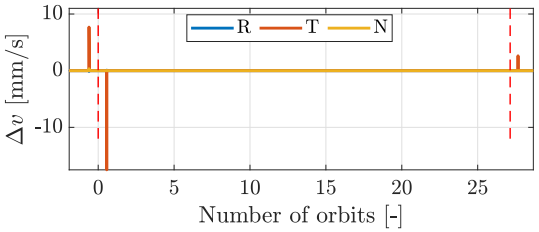

Fig. 9. Δv with FK constraints. TCAs are the red lines

lowers the orbit, causing the primary object to arrive earlier at the close approach, while the second burn adjusts the drift, timing the approach to the second conjunction differently. When the formation-keeping (FK) constraints are applied, the situation changes. As shown in Fig. 9, the first manoeuvre is executed half an orbit before the first conjunction, raising the orbit, while a second burn, half an orbit after the conjunction, lowers the semi-major axis and reverses the drift. Finally, after the second conjunction, the optimiser proposes a small burn to adjust the eccentricity vector. As expected, this different approach in disposing of the manoeuvres also leads to corresponding changes in the B-plane configurations as shown in Fig. 8. Fig. 10 represents the evolution of the mean relative semi-major axis in the two scenarios. Clearly, if no FK is embedded in the optimisation, the computed CAM causes a divergence of the parameter from its allowed values. The same is true for the mean relative eccentricity showed in Fig. 11: Without the constraint, the magnitude of the vector increases up to 52.24 m, whereas the optimiser can accurately target a value inside the 20 m-radius circle. Including the FK constraints allows for recovering an optimal formation with minimal Δv expenditure. Indeed, the total Δv goes from 1.898 cm/s to 4.026 cm/s when the constraints are included (112% relative increase). However, applying the FK constraint enables the spacecraft to return to its original state prior to the first conjunction.

In Table 1, the number of major iterations, total number of minor iterations, and computational times of the simulations are compared. It is clear that the simple scenarios with one conjunction, including the FK constraints, do not change the convergence speed significantly since the number of iterations remains the same, and the com-

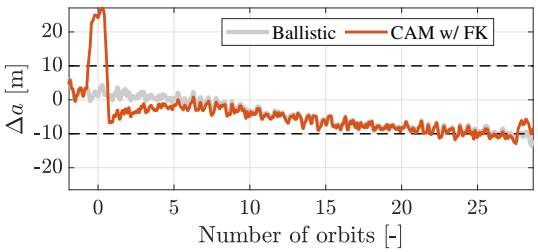

Fig. 10. Evolution of the mean relative semi-major axis in the multiple conjunction scenario.

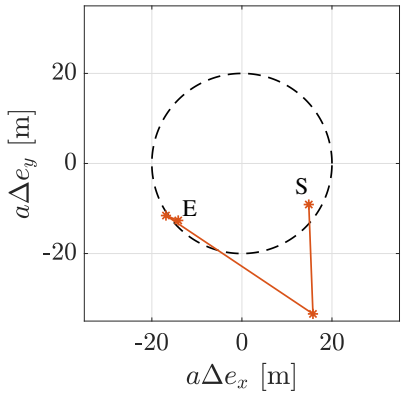

Fig. 11. Evolution of the mean relative eccentricity vector in the multiple conjunction scenario.

Table 1. Convergence properties of the performed simulations.

Scenario	n_{maj} [-]	n_{min} [-]	t_{comp} [s]
1 conj, w/o FK	3	4	1.33
1 conj, w/ FK	3	4	1.36
1 conj, tangential	3	4	1.30
2 conj, w/ FK	6	11	47.5

putation time is almost equal.

4.3 Validation

The testing scenarios in subsections 4.1 and 4.2 are validated using GSOC FD's flight-proven GRACE-FO formation monitoring tool. Specifically, the effect of the optimiser's computed CAMs and subsequent formation-keeping manoeuvres are analysed by simulating the formation state in the FDS before conjunctions. For Section 4.1, the optimiser's CAM closely matches the one executed by FD operators, differing by about 1 minute 20 seconds in timing but achieving a 13 % reduction in Δv for the same risk reduction. This discrepancy arises because operators tend to be more conservative, considering thruster performance forecasts based on manoeuvre history. Additionally, The post-CAM formation state is consistent with the results shown in Figures 5 and 6, with a Δa stabilizing around 22 meters and $a\Delta e = (27, -22)$ meters. Including the station-keeping manoeuvre computed by the optimiser produces the Δa and $a\Delta e$ formation evolution plots shown in Figures 12a and 13a. Notably, to meet the requirements, a second manoeuvre is performed about half an orbit after the TCA to reduce the eccentricity vector magnitude below 20 meters. The magnitude of this second Δv is 5% smaller than the CAM, providing a slight gain in Δa aiming at extending the relative along-track drift cycle as discussed in Section 2.2. Despite this, solar flux uncertainty continues to drive the drift pattern, resulting in conditions similar to those before the CAM. Referring to the testing scenario in 4.2, the computed manoeuvres are once again analysed using the formation monitoring tool to assess their impact. The pair of burns proposed by the optimiser, without considering the formation-keeping control, would have shortened the drift cycle and, at the same time, significantly increased the eccentricity vector beyond the allowed threshold. Figure 12b and 13b are instead showing the formation evolution when considering the FK constraints. Despite variations in the amplitude of oscillations, due to the high-fidelity algorithm implemented in the formation monitoring tool, the results align well with Fig. 10 and Fig. 11. The formation is, in fact, brought back to science configuration after the second conjunction. After the second conjunction, the formation successfully returns to its science configuration. The proposed formation-keeping manoeuvre slightly raises GF2, adjusting the eccentricity vector to approximately $(-5, -15)$ while also extending the along-track distance for about 20 more days before further control is needed.

4.3.1 Proposed Optimiser Operational Usage

We propose a practical example of how to include the optimiser in an operational pipeline for specialized CAM activities. As discussed in Section 2.3, although ground team coordination still constitutes the most time-consuming task, the optimiser can streamline manoeuvre planning. In fact, its primary strength lies in computational efficiency, and when tailored to a specific mission, it greatly enhances automation, reducing human intervention. Usually, in the first instance, operators compute an avoidance manoeuvre that would bring the PoC to a safe value, and then, secondly, they analyse how this would affect the evolution of the formation in the short term. The optimiser can already provide this information in advance, and an automatic periodic process, as proposed in Fig. 14, can be put in place. Specifically, the FDS can feed the optimiser with the latest OD of the formation in the form of ephemerides, taking advantage of the process described in Section 3.2.1. Additionally, it can also provide informa-

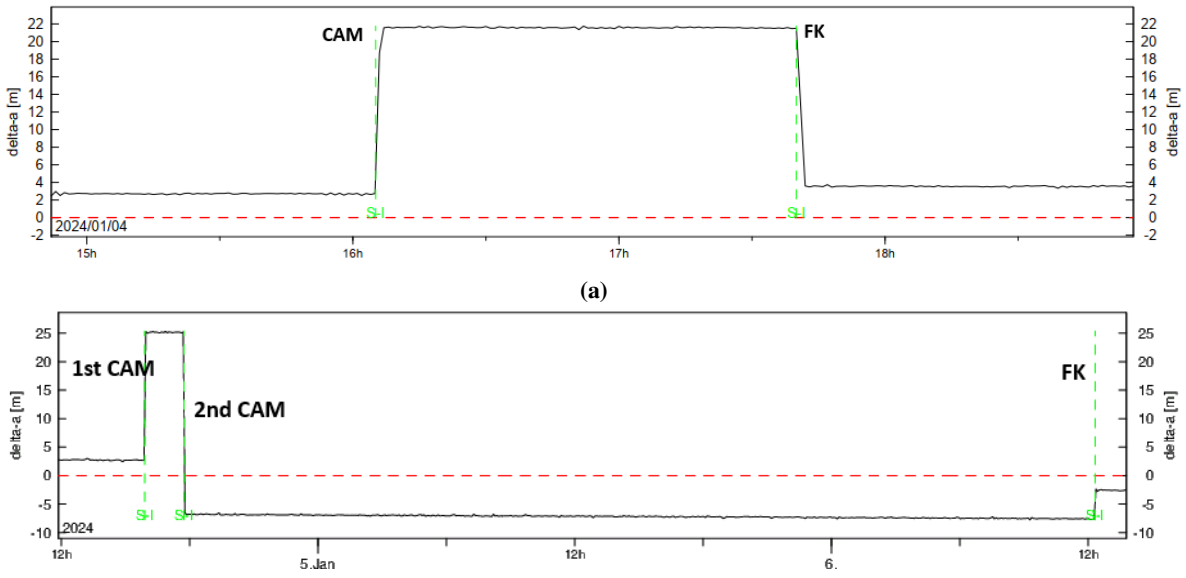

Fig. 12. GRACE-FO formation monitoring tool: Δa evolution for (a) the single encounter scenario and (b) the multiple encounter scenario

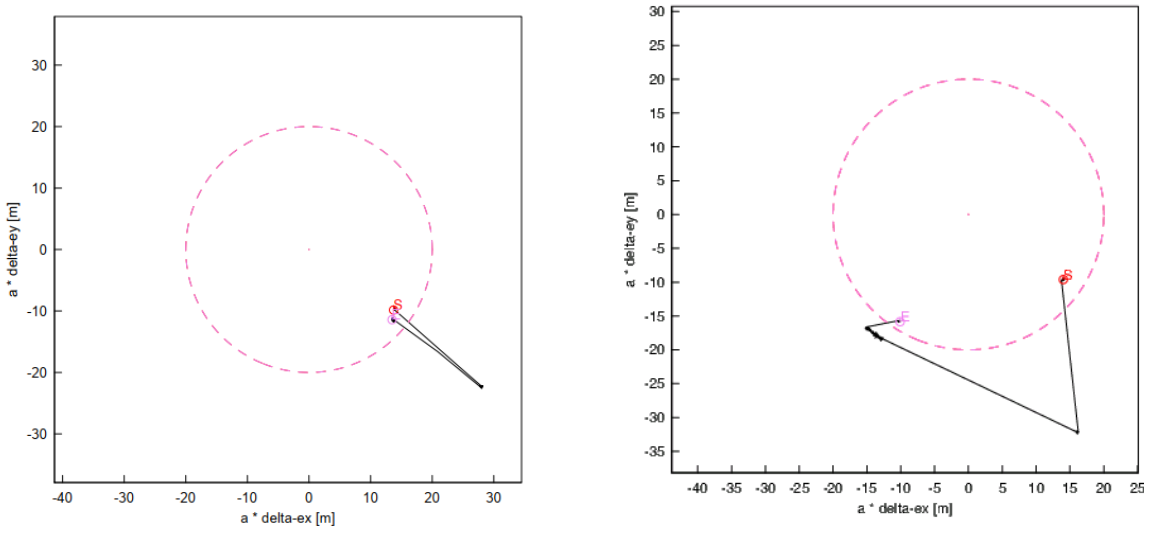

Fig. 13. GRACE-FO formation monitoring tool: $a\Delta e$ evolution for (a) the single encounter scenario and (b) the multiple encounter scenario

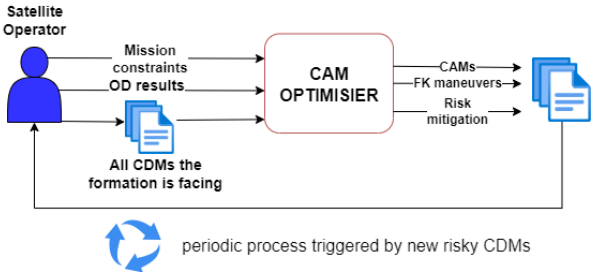

Fig. 14. Proposed workflow on how to use the optimiser for Collision avoidance operations.

tion, via its collision avoidance system, about all the close approaches that the formation is facing in the next 7 days and a mission-related constraint configuration file guiding the optimiser's calculations. The optimiser then returns CAMs, possible FK manoeuvres and risk reduction plots. Operators can review and validate these solutions before uploading them to the spacecraft.

5. Conclusions and Future Work

This work builds on the authors' previously established line of research that focuses on computing a collision avoidance manoeuvre (CAM) using a sequential convex program (SCP) approach. Specifically, the proposed methodology is enhanced by tailoring the algorithm for a real mission scenario, namely the Gravity Recovery and Climate Experiment-Follow-On (GRACE-FO), operated by DLR. This marks the first step toward making the methodology applicable and usable in daily operations.

The original non-convex problem is convexified and solved iteratively in the framework of SCP. To do this, the collision risk is estimated via the Chan approximation of the probability of collision (PoC). This allows for the linearization of the squared Mahalanobis distance to formulate the collision avoidance constraint as an elliptical keep-out zone. The operational effectiveness of the algorithm is further enhanced by using custom ephemerides when convexifying the dynamics, ensuring a high level of accuracy. Moreover, the proposed approach couples the CAM execution with formation-keeping (FK) constraints, which are fundamental in the considered scenario because of the nature of the mission.

The optimiser is tested on two real conjunction scenarios encountered by GRACE-FO in January 2024. Specifically, two cases are presented: a single close approach and a scenario involving multiple consecutive conjunctions. For both cases, the computed manoeuvres that combine CAM and FK are validated using DLR's flight-proven formation monitoring software, demonstrating that the proposed solutions could have been realistically implemented.

The work concludes with a brief proposal on how the solver could be integrated into the collision avoidance operations pipeline. In future work, the authors plan to further enhance the methodology by introducing the capability to propose FK manoeuvres on both satellites composing the formation. Additionally, efforts will focus on consolidating testing and improving the optimiser's formation monitoring algorithms to enable long-term analysis of the satellites' formation.

References

[1] ESOC. ESA's Annual Space Environment Report. Technical report, ESA, 2023.

[2] Saika Aida. Conjunction risk assessment and avoidance maneuver planning tools. In *6th International Conference on Astrodynamics Tools and Techniques*, Darmstadt, Germany, March 2016.

[3] Zeno Pavanello, Laura Pirovano, and Roberto Armellin. Long-Term Fuel-Optimal Collision Avoidance Maneuvers with Station-Keeping Constraints. *Journal of Guidance, Control, and Dynamics*, pages 1–17, aug 2024. ISSN 0731-5090. doi: 10.2514/1.G007839.

[4] Zeno Pavanello, Laura Pirovano, Roberto Armellin, Andrea De Vittori, and Pierluigi Di Lizia. A Convex Formulation for Collision Avoidance Maneuver Strategies During Low-Thrust Phases. In *AIAA SciTech Forum*, number January, pages 1–19. Orlando, Florida, 2024. doi: 10.2514/6.2024-0844.

[5] Zeno Pavanello, Laura Pirovano, Roberto Armellin, Andrea De Vittori, and Pierluigi Di Lizia. A Convex Optimization Method for Multiple Encounters Collision Avoidance Maneuvers. In *AIAA SciTech Forum*, number January, pages 1–17. Orlando, Florida, 2024. doi: 10.2514/6.2024-0845.

[6] Zhenbo Wang and Michael J. Grant. Minimum-Fuel Low-Thrust Transfers for Spacecraft: A Convex Approach. *IEEE Transactions on Aerospace and Electronic Systems*, 54(5):2274–2290, 2018. ISSN 15579603. doi: 10.1109/TAES.2018.2812558.

[7] Behçet Açıkmeşe and Lars Blackmore. Lossless convexification of a class of optimal control problems with non-convex control constraints. *Automatica*, 47(2):341–347, 2011. ISSN 0005-1098. doi: https://doi.org/10.1016/j.automatica.2010.10.037.

[8] Roberto Armellin. Collision avoidance maneuver optimization with a multiple-impulse convex formulation. *Acta Astronautica*, 186:347–362, sep 2021. ISSN 00945765. doi: 10.1016/j.actaastro.2021.05.046.

[9] Yuanqi Mao, Daniel Dueri, Michael Szmuk, and Behçet Açıkmeşe. Successive Convexification of Non-Convex Optimal Control Problems with State Constraints. In *IFAC*, volume 50, pages 4063–4069. Elsevier B.V., jul 2017. doi: 10.1016/j.ifacol.2017.08.789.

[10] Luis Sánchez and Massimiliano Vasile. Constrained Optimal Collision Avoidance Manoeuvre Allocation under Uncertainty for Subsequent Conjunction Events. In *72nd International Astronautical Congress, IAC*, volume A6. Dubai, United Arab Emirates, 2021.

[11] Alessandro Morselli, Roberto Armellin, Pierluigi Di Lizia, Franco Bernelli Zazzera, and F. Bernelli-Zazzera. Collision avoidance maneuver design based on multi-objective optimization. In *AIAA/AAS Astrodynamics Specialist Conference 2014*, volume 152, pages 1819–1838. San Diego, California, 2014. ISBN 9780877036111.

[12] Joseph B. Mueller, Paul R. Griesemer, and Stephanie J. Thomas. Avoidance maneuver planning incorporating station-keeping constraints and automatic relaxation. *Journal of Aerospace Information Systems*, 10(6):306–322, jun 2013. ISSN 23273097. doi: 10.2514/1.54971.

[13] Richard P. Kornfeld, Bradford W. Arnold, Michael A. Gross, Neil T. Dahya, William M. Klipstein, Peter F. Gath, and Srinivas Bettadpur. Grace-fo: The gravity recovery and climate experiment follow-on mission. *Journal of Spacecraft and Rockets*, 56(3):931–951, 2019. doi: 10.2514/1.A34326.

[14] Simone D'Amico and Oliver Montenbruck. Proximity operations of formation-flying spacecraft using an eccentricity/inclination vector separation. *Journal of Guidance, Control, and Dynamics*, 29(3):554–563, 2006. doi: https://doi.org/10.2514/1.15114.

[15] S. D'Amico. *Autonomous Formation Flying in Low Earth Orbit*. PhD thesis, Technical University of Delft, 2010.

[16] Russell Patera. Satellite Collision Probability for Non-Linear Relative Motion. In *AIAA/AAS Astrodynamics Specialist Conference and Exhibit*, volume 26, Reston, Virigina, aug 2002. American Institute of Aeronautics and Astronautics. doi: 10.2514/6.2002-4632.

[17] Kyle T Alfriend, Maruthi R Akella, Joseph Frisbee, James L Foster, Deok-Jin Lee, and Matthew Wilkins. Probability of collision error analysis. *Space Debris*, 1999. doi: https://doi.org/10.1023/A:1010056509803.

[18] Javier Hernando-Ayuso and Claudio Bombardelli. Low-thrust collision avoidance in circular orbits. *Journal of Guidance, Control, and Dynamics*, 44(5):983–995, may 2021. ISSN 15333884. doi: 10.2514/1.G005547.

[19] Andrea De Vittori, Maria Francesca Palermo, Pierluigi Di Lizia, and Roberto Armellin. Low-Thrust Collision Avoidance Maneuver Optimization. *Journal of Guidance, Control, and Dynamics*, 45(10):1815–1829, oct 2022. ISSN 15333884. doi: 10.2514/1.G006630.

[20] Shuo Zhang, Tuo Fu, Defeng Chen, and Huawei Cao. Satellite instantaneous collision probability computation using equivalent volume cuboids. *Journal of Guidance, Control, and Dynamics*, 43(9):1757–1763, 2020. ISSN 15333884. doi: 10.2514/1.G004711.

[21] Ken Chan. International Space Station Collision Probability. *The Aerospace Corporation, Chantilly, VA, USA*, 6(2):307–314, 2009.

[22] Salvatore Alfano. Review of conjunction probability methods for short-term encounters. In *Advances in the Astronautical Sciences*. 2007. ISBN 9780877035411.

[23] Danylo Malyuta, Taylor P. Reynolds, Michael Szmuk, Thomas Lew, Riccardo Bonalli, Marco Pavone, and Behçet Açıkmeşe. Convex Optimization for Trajectory Generation: A Tutorial on Generating Dynamically Feasible Trajectories Reliably and Efficiently. *IEEE Control Systems*, 42(5):40–113, oct 2022. ISSN 1066-033X. doi: 10.1109/MCS.2022.3187542.

[24] Nicolò Bernardini, Nicola Baresi, and Roberto Armellin. State-dependent trust region for successive convex programming for autonomous spacecraft. *Astrodynamics*, pages 1–20, apr 2024. ISSN 2522-008X. doi: 10.1007/s42064-024-0200-1.

[25] Matteo Losacco, Alberto Fossà, and Roberto Armellin. Low-Order Automatic Domain Splitting Approach for Nonlinear Uncertainty Mapping. *Journal of Guidance, Control, and Dynamics*, pages 1–20, jan 2024. ISSN 0731-5090. doi: 10.2514/1.G007271.

[26] Yuanqi Mao and Behcet Acikmese. SCvx-fast: A Superlinearly Convergent Algorithm for A Class of

Non-Convex Optimal Control Problems. *ArXiv*, 2112, nov 2021.

[27] Claudio Bombardelli and Javier Hernando-Ayuso. Optimal impulsive collision avoidance in low earth orbit. In *Journal of Guidance, Control, and Dynamics*, volume 38, pages 217–225, feb 2015. doi: 10.2514/1.G000742.